Front. Environ. Sci. Eng. 2024, 18(3): 37
https://doi.org/10.1007/s11783-024-1797-2

RESEARCH ARTICLE

Magnetic Co-doped 1D/2D structured γ-Fe_2O_3/MoS_2 effectively activated peroxymonosulfate for efficient abatement of bisphenol A via both radical and non-radical pathways

Junge Xu[1], Dong Wang[1], Die Hu[2], Ziwei Zhang[1], Junhong Chen[1], Yingmu Wang (✉)[1], Yifeng Zhang (✉)[3]

1 College of Civil Engineering, Fuzhou University, Fuzhou 350116, China
2 China Nuclear Power Engineering Co., Ltd., Shenzhen 518120, China
3 Department of Environmental & Resource Engineering, Technical University of Denmark, Lyngby DK-2800, Denmark

HIGHLIGHTS

- Magnetic Co-γ-Fe_2O_3/MoS_2 were prepared via facile hydrothermal methods.
- Doping γ-Fe_2O_3 with cobalt greatly increased PMS activation for BPA abatement.
- The compounding of MoS_2 significantly enhanced the stability of the catalyst.
- Hybrid radical-nonradical pathways acted for effective degradation of BPA.
- The toxicity of intermediates was lower than BPA via T.E.S.T analysis.

GRAPHIC ABSTRACT

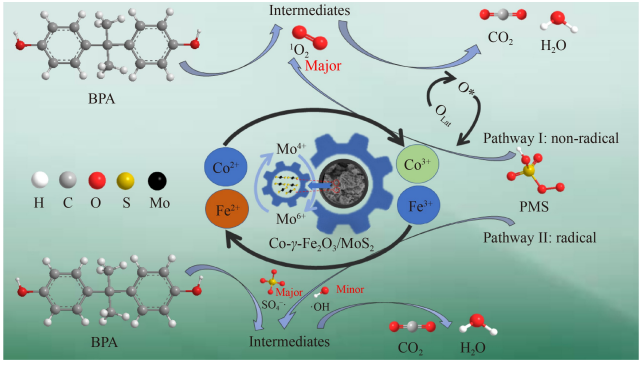

ARTICLE INFO

Article history:
Received 1 March 2023
Revised 5 October 2023
Accepted 7 October 2023
Available online 10 December 2023

Keywords:
Magnetic Co-γ-Fe_2O_3/MoS_2
Hydrothermal method
Bisphenol A
Degradation pathways
Toxicity analysis

ABSTRACT

Iron-based catalysts have been widely used to treat refractory organic pollutants in wastewater. In this paper, magnetic Co-γ-Fe_2O_3 was synthesized by a facile tartaric acid-assisted hydrothermal method, and Co-γ-Fe_2O_3/MoS_2 nanocomposite catalyst was obtained via *in situ* growth of MoS_2 nanosheets on Co-γ-Fe_2O_3 nanoparticles. The nanocomposite catalysts were used to decompose bisphenol A (BPA) by activating peroxymonosulfate (PMS). It was shown that only 0.15 g/L catalyst and 0.5 mmol/L PMS degraded 10 mg/L of BPA (99.3% within 10 min) in the pH range of 3–9. PMS was activated due to redox cycling among the pairs Co(III)/Co(II), Fe(III)/Fe(II), and Mo(VI)/Mo(IV). Quenching experiments and electron paramagnetic resonance spectroscopy demonstrated that both radical and non-radical pathways were involved in BPA degradation, in which active radical sulfate radical and non-radical singlet oxygen were the main reactive oxygen species. Ten intermediates were identified by liquid chromatography-coupled mass spectrometry, and three possible BPA degradation pathways were proposed. The toxicity of several degradation intermediates was lower, and Co-γ-Fe_2O_3/MoS_2 exhibited excellent reusability and could be magnetically recovered.

1 Introduction

In recent years, bisphenol A (BPA) has become one of the most broadly utilized and consumed chemicals for plasticizers, hardeners, and adhesives in plastic products (Wang et al., 2020). However, after entering aquatic

✉ Corresponding authors
E-mails: wangym@fzu.edu.cn (Y. Wang); yifz@dtu.dk (Y. Zhang)

Special Issue—Cutting-edge Research Under the European Green Deal: Water Resources Engineering (Responsible Editors: Yifeng Zhang, Elvis Genbo Xu, Xing Yang & Liwen Xiao)

environments and subsequent exposure to human beings and animals, BPA interacts with their endocrine receptors and impacts their reproduction, development, and neurological and immune systems (Gao et al., 2021; Liu et al., 2022). BPA has been frequently detected in aquatic ecosystems at concentrations of up to 21 μg/L (Sun et al., 2022), which has raised growing public concern. Hence, the removal of BPA has become an urgent problem.

Among the techniques for the removal of bio-recalcitrant contaminants, advanced oxidation processes based on sulfate radicals ($SO_4^{\bullet-}$) generated by activating persulfates have attracted increasing research attention. Compared with hydroxyl radicals (•OH), $SO_4^{\bullet-}$ exhibits some advantages, including: 1) a higher oxidizing potential (E_0 = 2.5–3.1 V *vs.* 1.8–2.7 V for •OH) (Pan et al., 2018; Sun et al., 2022), 2) a longer half-life (30–40 μs *vs.* < 1 μs for •OH), and 3) applicability over a wider pH range. Regarding persulfates, peroxymonosulfate (PMS) is a better oxidant than peroxydisulfate (PDS) due to its asymmetric structure and longer superoxide O–O bond, which is more easily activated by the catalyst to produce reactive oxygen species (ROSs) (Duan et al., 2018). Notably, several methods have been used to activate PMS, mainly including heat-activated (Liu et al., 2023), ultraviolet-activated (Lu et al., 2019), ultrasound-activated (Xu et al., 2020), and transition metal-based heterogeneous activation methods (Lu et al., 2022). Among them, transition metal-based (e.g., Fe, Co, and Cu) heterogeneous activation allows catalysts to be developed that show magnetic recovery, excellent catalytic performance, and application over a broad pH range (Chen et al., 2019b; Long et al., 2023). Recently, iron-based catalysts, especially one-dimensional (1D) γ-Fe_2O_3, have a high natural abundance, eco-friendliness, stability, and ease of recovery (Niu et al., 2021; Wang et al., 2022b; Zhao et al., 2022). However, the application of iron-based catalysts is usually limited due to the low conversion of Fe^{3+} to Fe^{2+} (Mao et al., 2018). Ma et al. (2019) found that rhodamine B could barely be removed by γ-Fe_2O_3/PMS within 150 min. Compounding γ-Fe_2O_3 with other metal oxides or doping other transition metal ions on γ-Fe_2O_3 are efficient ways to enhance the catalytic performance of γ-Fe_2O_3. Notably, the integration of cobalt ions (Co^{2+}) or cobalt oxide can generate one of the most effective activators for PMS. Zhu et al. (2019a) reported that atrazine degradation was more efficient in the Co-doped mesoporous $FePO_4$/PMS system than in the $FePO_4$/PMS system. However, these activation systems were susceptible to the leaching of toxic Co^{2+} after oxidation (Duan et al., 2018; Zhu et al., 2019a; Sun et al., 2020a). Additionally, earlier investigations demonstrated that the stability and recoverability of the Co-based catalysts require improvements, and the ROS generation mechanism during the reaction requires further investigation (Ma et al., 2019). Molybdenum sulfide (MoS_2), a transition metal dichalcogenide with a two-dimensional (2D) layered structure with high electron mobility, accelerated the production of ROSs (Xie et al., 2022; Yan et al., 2022). Moreover, it prevented the leaching of metal ions and thereby enhanced the stability and catalytic performance of the catalyst for recycling. He et al. (2022b) used a $SrCoO_3$/$MnFe_2O_4$/MoS_2 nanocomposite to remove levofloxacin (LVF) by activating PMS under visible light, and the removal efficiency of LVF remained at 85.2% after five cycles. It has been demonstrated that catalyst performance for the decomposition of different target pollutants is also connected to the activation mechanism of PMS. Recently, apart from radical pathway activation, several studies have demonstrated that PMS can also be activated via non-radical pathways, such as the generation of single oxygen ($^1O_2$) with a gentle oxidative capacity (2.2 V) and a high selectivity for attacking organic pollutants (Zhu et al., 2019b).

Considering the excellent properties of MoS_2, the integration of Co-γ-Fe_2O_3 and MoS_2 is expected to enhance the cyclic activity and stability of the material, and the novel magnetic nanomaterial Co-γ-Fe_2O_3/MoS_2 was fabricated via a two-step hydrothermal method in this work. The structure, morphology, surface composition, and magnetic properties of the compound materials were characterized by various techniques such as X-ray diffraction (XRD), transmission electron microscopy (TEM), scanning electron microscopy (SEM), and vibrating sample magnetometry (VSM). Co-γ-Fe_2O_3/MoS_2/PMS was employed to remove BPA in aqueous solution. The effects of reaction systems, initial pH, catalyst dosage, PMS concentration, coexisting anions, and natural organic matter on BPA degradation were investigated and discussed. As expected, Co-γ-Fe_2O_3/MoS_2 demonstrated excellent degradation of BPA and enhanced cycling stability. Furthermore, the main active species were investigated by quenching experiments and electron paramagnetic resonance (EPR) analysis. The potential decomposition pathways of BPA were proposed according to liquid chromatography-coupled mass spectrometry (LC-MS), and the toxicity of the substances formed during degradation was explored by a toxicity estimation software tool (T.E.S.T).

2 Materials and methods

2.1 Materials

Cobalt nitrate hexahydrate ($Co(NO_3)_2{\cdot}6H_2O$, 99%), iron nitrate nonahydrate ($Fe(NO_3)_3{\cdot}9H_2O$, 99.9%), ammonium molybdate tetrahydrate ($(NH_4)_6Mo_7O_{24}{\cdot}4H_2O$, 99%), thiourea ($CH_4N_2S$, 99%), ethanol ($C_2H_6O$, 75%), *p*-benzoquinone (*p*-BQ, 97%), sodium nitrate ($NaNO_3$),

sodium sulfate (Na_2SO_4), sodium chloride (NaCl), and sodium bicarbonate ($NaHCO_3$) were purchased from Sinopharm Chemical Reagent Co., Ltd. (Shanghai, China). Polyethylene glycol 400 (PEG 400, $H(OCH_2CH_2)_nOH$), tartaric acid ($C_4H_6O_6$), bisphenol A (BPA, $C_{14}H_{18}N_4O_3$, 99%), methanol (MeOH, CH_4O), *tert*-butyl alcohol (TBA, $C_4H_{10}O$), L-histidine ($C_6H_9N_3O_2$), and acetonitrile (CH_3CN) were purchased from Aladdin Chemical Reagent Co., Ltd. (Shanghai, China). Hydrochloric acid (HCl) and sodium hydroxide (NaOH) were purchased from Tianjin Fuchen Chemical Reagent Co., Ltd. (Tianjin, China). Acetonitrile and methanol were HPLC grade, and the remaining chemicals were analytical grade purity. All chemicals were used without further purification.

2.2 Catalyst synthesis

The magnetic Co-γ-Fe_2O_3 and Co-γ-Fe_2O_3/MoS_2 composites were fabricated via hydrothermal methods. Co-γ-Fe_2O_3 was synthesized by using environment-friendly and readily available tartaric acid as an assisting agent. The detailed preparation processes are as follows.

2.2.1 Preparation of Co-γ-Fe_2O_3

The Co-γ-Fe_2O_3 complex was obtained by a simple hydrothermal method based on the synthesis method of Liu et al. (2019). The schematic diagram of the synthesis is shown in Fig. S1. Briefly, $Fe(NO_3)_3{\cdot}9H_2O$ was dissolved in a solution of PEG 400 in deionized water. Then, magnetic stirring was performed, while tartaric acid and $Co(NO_3)_2{\cdot}6H_2O$ were added to the solution. The optimal ratio of Co to Fe for BPA degradation was 3: 100 (Text S1 and Fig. S2). The mixture was moved into a Teflonlined autoclave and kept at 180 °C for 9 h. Finally, the black products were washed multiple times with deionized water and anhydrous ethanol and then dried to gain the final products. In this work, tartaric acid was chosen as an auxiliary synthesis material because of its low toxicity and low cost, as well as its ability to provide the carboxyl groups necessary for the reaction (Golestani et al., 2018).

2.2.2 Preparation of Co-γ-Fe_2O_3/MoS_2

A novel hydrothermal method was adopted for the *in situ* loading of MoS_2 nanosheets on the synthesized Co-γ-Fe_2O_3 nanomaterials. Specifically, $(NH_4)_6Mo_7O_{24}{\cdot}4H_2O$ and CH_4N_2S were dissolved in 30 mL of deionized water under ultrasound. Co-γ-Fe_2O_3 powder was mixed into the above solution, and the obtained black suspension was ultrasonicated intermittently. Then, the mixture was transferred into a 50-mL Teflonlined autoclave and heated at 180 °C for 10 h. After the reaction, the black precipitate was separated by centrifugation, washed several times with deionized water and anhydrous ethanol, and finally dried at 60 °C for 12 h. Pure MoS_2 was obtained via a similar method.

2.3 Catalyst characterization

XRD was performed using Cu Kα radiation to observe the crystal structure of the catalysts (Bruker AXS, Germany). X-ray photoelectron spectroscopy (XPS; ESCALAB Xi^+, Thermo Fisher Scientific, USA) was conducted to identify the chemical components on the catalyst surface before and after the reaction. To study the surface morphology and obtain the element maps of the catalysts, field emission scanning electron microscopy (FE-SEM; GeminiSEM 300, ZEISS, Germany) and high-resolution transmission electron microscopy (HRTEM; FEI Tecnai F30, USA) were employed. The zeta potentials of the catalysts were determined with a nanoparticle potentiometer (Malvern, Nano-ZS90, UK). Magnetic properties were measured at room temperature by VSM (Quantum Design, PPMS-9, USA). The surface functional groups of the samples were identified and analyzed by Fourier-transform infrared (FTIR) spectroscopy.

2.4 Evaluation methods

Details of the used evaluation methods regarding the determination of BPA degradation efficiency, investigation of major ROSs, assessment of catalyst reusability, identification of generated intermediates, possible degradation pathways, and toxicity of intermediates are provided in Text S2.

3 Results and discussion

3.1 Characteristics of photocatalysts

3.1.1 Structural features

The XRD patterns of pure MoS_2, γ-Fe_2O_3, Co-γ-Fe_2O_3, and Co-γ-Fe_2O_3/MoS_2 are depicted in Fig. 1(a). The diffraction peaks of Co-doped catalyst at 2θ = 18.44°, 29.74°, 35.44°, 42.94°, 53.50°, 57.08°, and 62.48° corresponded to the (111), (220), (311), (440), (422), (511), and (400) crystal planes of γ-Fe_2O_3, respectively, consistent with data in JCPDS No. 39-1346. No characteristic peaks of Co or Co-based compounds were observed, indicating the atomic dispersion of Co species in γ-Fe_2O_3 (Bai et al., 2020). Co-γ-Fe_2O_3/MoS_2 retained the characteristic peaks of γ-Fe_2O_3. However, the intensity of the corresponding peaks was reduced, indicating that loading MoS_2 did not affect the crystal

shape and phase of γ-Fe_2O_3, but it did decrease the crystallinity of the oxide (He et al., 2022b). No obvious peaks of MoS_2 were observed, most likely due to its low crystallinity, low content, and high diffusion of MoS_2 on the Co-γ-Fe_2O_3 surface (Zheng et al., 2019; Zhou et al., 2020).

3.1.2 Morphological analysis

The microscopic features of the compounds were observed by SEM. Figure 1(b) displays the SEM image of Co-γ-Fe_2O_3, which consisted of fine nanoparticles with an average particle size of about 20.88 nm. The morphology of Co-γ-Fe_2O_3/MoS_2 showed that Co-γ-Fe_2O_3 nanoparticles were well combined with 2D MoS_2 nanosheets (Fig. 1(c)), indicating that MoS_2 was successfully anchored to the surface of Co-γ-Fe_2O_3 (He et al., 2022a). A previous study showed that ultra-thin 2D nanosheets could expose sufficient active sites and reduce the charge diffusion length to accelerate charge carrier transfer, which facilitated the improvement of catalyst activity (Geng et al., 2021). Furthermore, the MoS_2 nuclei were grown *in situ* on the Co-γ-Fe_2O_3 nanoparticles in the hydrothermal reaction, and the MoS_2 nanosheets were also loaded with Co-γ-Fe_2O_3 nanoparticles. This generated strong interactions between them and promoted the formation of a favorable heterojunction at the interface, ensuring the stability of the nanometer-sized thin flake flower-like structure.

In addition, HRTEM and FTIR spectroscopy were performed to reveal more definite evidence for the nano-heterostructures of Co-γ-Fe_2O_3/MoS_2. As shown in Fig. 1(d), the samples consisted of nearly spherical nanoparticles, which indicated the successful synthesis of γ-Fe_2O_3 (Li et al., 2015). Furthermore, it could be observed that some nanoparticles were attached to the nanosheets. The HRTEM images in Figs. S3(a)–S3(c) display the narrow interface between the two composites. The lattice spacings 0.251, 0.241, and 0.295 nm were attributed to the (311), (222), and (220) crystal planes of γ-Fe_2O_3 (Ge et al., 2021; Wu et al., 2022). The MoS_2 nanosheets exhibited lattice spacings of 0.614 and 0.227 nm, which were attributed to the (002) and (103) crystal planes, respectively (Zhang et al., 2018), compatible with the XRD results. Besides, as demonstrated in Fig. S4, the surface functional groups of γ-Fe_2O_3, Co-γ-Fe_2O_3, MoS_2, and Co-γ-Fe_2O_3/MoS_2 were studied by FTIR spectroscopy. The small peak at about 685 cm^{-1} was related to the stretching of the Co–O bond in Co-γ-Fe_2O_3 (Sakthi Athithan et al., 2021). In addition, the peaks located at about 1089, 1629, and 2919 cm^{-1} were assigned to C–O–C, C–O, and C–H bond vibrations of PEG, respectively (Abareshi and Salehi, 2022; Li et al., 2022b). The peak near 699 cm^{-1} was assigned to the Mo–O bonds of MoS_2 (Ikram et al., 2020). The small peak at about 1126 cm^{-1} was assigned to the S=O

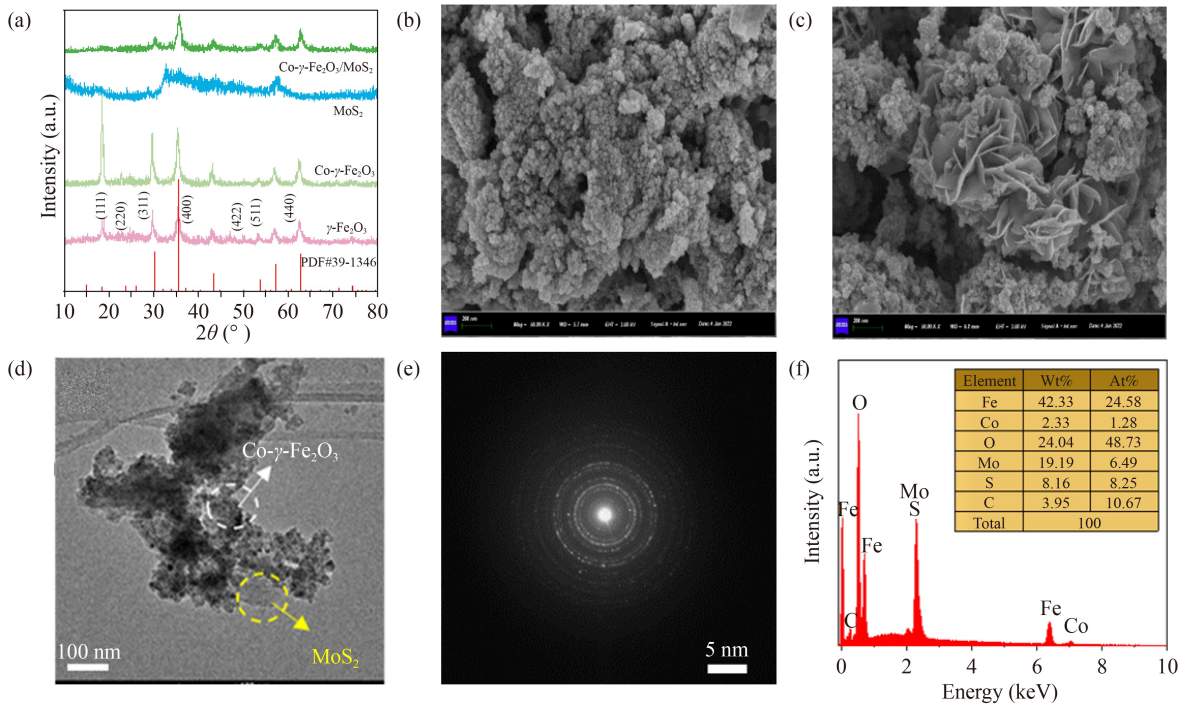

Fig. 1 (a) XRD patterns of γ-Fe_2O_3, MoS_2, Co-γ-Fe_2O_3 and Co-γ-Fe_2O_3/MoS_2. SEM images of (b) Co-γ-Fe_2O_3 and (c) Co-γ-Fe_2O_3/MoS_2. (d) TEM images of Co-γ-Fe_2O_3/MoS_2, (e) SAED image of Co-γ-Fe_2O_3/MoS_2 and (f) EDS images of Co-γ-Fe_2O_3/MoS_2.

functional group, while the broad band at ~3441 cm^{-1} was ascribed to the symmetric stretching vibration of O–H (Zhang et al., 2023). All of the above characteristic peaks were also present in the spectra of the composite catalyst Co-γ-Fe_2O_3/MoS_2, indicating the presence of both Co-γ-Fe_2O_3 and MoS_2. In Fig. 1(e), the selected area electron diffraction (SAED) plot of Co-γ-Fe_2O_3/MoS_2 displays a set of concentric rings, and the rings and shiny spots matched the reflections of γ-Fe_2O_3 nanoparticles during the synthesis of Co-γ-Fe_2O_3/MoS_2 (Ge et al., 2021), indicating that the sample was composed of polycrystals (Xu et al., 2011). The elemental composition of Co-γ-Fe_2O_3/MoS_2 is displayed in Fig. 1(f). The sample consisted of six elements, Fe, Co, O, Mo, S, and C, with percentages of 24.58%, 1.28%, 48.73%, 6.49%, 8.25%, and 10.67%, respectively. The presence of C was attributed to the use of Lacey carbon carriers during the test and the high C content in the precursors PEG 400 and tartaric acid (Liu et al., 2021a). These results demonstrated the successful doping of Co and compounding of MoS_2.

3.1.3 Elemental surface composition analysis

To further identify the surface composition and chemical states of the samples, the XPS spectra of the composites were recorded, as displayed in Figs. 2(a)–2(f). The XPS survey spectrum of the Co-γ-Fe_2O_3/MoS_2 composite is displayed in Fig. 2(a), and all constituent elements of the catalyst (i.e., Fe, Co, O, Mo, S, and C) were examined and characterized. In Fig. 2(b), the binding energies at 724.5 and 710.9 eV were characteristic double peaks of Fe^{3+} $2p_{1/2}$ and Fe^{3+} $2p_{3/2}$, respectively (Flak et al., 2018). The peaks at 719.0 and 733.0 eV were assigned to satellite peaks and were also characteristic features of Fe^{3+} rather than Fe^{2+} (Wang et al., 2022c). The variation of binding energy between different orbitals was due to spin-orbit coupling and was equivalent to that of γ-Fe_2O_3 (Su et al., 2022). Therefore, the combination of XRD and XPS proved that the catalyst was γ-Fe_2O_3 rather than Fe_3O_4. The Co 2p XPS spectra (Fig. 2(c)) displayed two peaks at binding energies of 780.5 and 795.9 eV, which corresponded to Co $2p_{3/2}$ and Co $2p_{1/2}$, respectively (Barik et al., 2017). The peaks at 780.3 and 795.5 eV in the Co 2p spectrum were attributed to Co^{2+} (Guo and Hu, 2022), while the peaks at 782.4 and 797.1 eV originated from Co^{3+}. Furthermore, the peaks at 787.1 eV and 803.2 eV were identified as satellite peaks of Co^{3+} and Co^{2+}, respectively (Li et al., 2022a). In Fig. 2(d), the peaks at 228.7 and 232.1 eV were attributed to the Mo^{4+} $3d_{5/2}$ and Mo^{4+} $3d_{3/2}$ orbitals of MoS_2. The peak at 225.9 eV was assigned to the S 2s orbital of MoS_2, and the peak at 235.8 eV originated from Mo^{6+} $3d_{3/2}$, which may indicate the presence of MoO_3 produced by partial oxidation of MoS_2 in air atmosphere (Qi et al., 2019). In the S 2p spectrum, the peaks at 161.5 and 162.7 eV (Fig. 2(e)) were attributed to S $2p_{3/2}$ and S $2p_{1/2}$ (Yue et al., 2022). These results revealed that MoS_2 was synthesized successfully and exhibited excellent complexation with Co-γ-Fe_2O_3. The O 1s XPS spectrum of the catalyst could be deconvoluted into two components (Fig. 2(f)) at 530.1 and 531.4 eV, which were ascribed to lattice oxygen (O_L) and highly oxidizing oxygen (O^{2-}, O^-, or –OH), respectively (Zeng et al., 2018). Additionally, the peak at 533.2 eV corresponded to physically adsorbed oxygen (O_{ads}) on the composite (Zhang et al., 2018).

3.1.4 Analyses of textural, surface charge, and magnetic properties

The specific surface areas (S_{BET}) and porous structures of synthesized Co-γ-Fe_2O_3 and Co-γ-Fe_2O_3/MoS_2 were studied by Brunauer-Emmett-Teller (BET) analysis. The obtained N_2 adsorption-desorption isotherms and the Barrett-Joyner-Halenda (BJH) porous structure distribution curves are displayed in Figs. S5(a) and S5(b). In the relative pressure (P/P_0) range of 0.1–0.9, all composites exhibited type IV isotherms with H3 hysteresis loops, indicating the mesoporosity of the composites (Sarkar et al., 2022a). Compared with Co-γ-Fe_2O_3 (S_{BET} = 33.42 m^2/g), the surface area of Co-γ-Fe_2O_3/MoS_2 was larger (45.26 m^2/g) (Fig. S5(a)). The relevant pore diameter distribution of composites peaked at about 10 nm (Fig. S5(b)), and the average pore size of Co-γ-Fe_2O_3/MoS_2 (11.36 nm) was slightly larger than Co-γ-Fe_2O_3 (10.09 nm). Additionally, the total pore capacity of Co-γ-Fe_2O_3/MoS_2 was higher than that of Co-γ-Fe_2O_3, which could be attributed to the uniform distribution of the Co-γ-Fe_2O_3 nanoparticles on the surface of MoS_2. The porous structure of Co-γ-Fe_2O_3/MoS_2 exhibited better adsorption performance and provided more active sites exposed to the material surface, which contributed to the degradation of the BPA molecules.

The variation in the surface zeta potential of the composite with solution pH is displayed in Fig. S5(c), indicating that the zero point charge (pH_{zpc}) of Co-γ-Fe_2O_3/MoS_2 was 4.25. Under acidic conditions (pH < 4.25), the material had a positive charge because of the protonation of the surface functional groups, and the negative charges at pH > 4.25 due to metal oxides being hydroxylated. Additionally, the surface zeta potential of Co-γ-Fe_2O_3/MoS_2 changed from 24.2 mV (pH 2) to −35.8 mV (pH 11) (Luciano et al., 2020).

The magnetic hysteresis loops of the samples were analyzed by using VSM, and the related curves were presented in Fig. S5(d). The magnetic moment of Co-γ-Fe_2O_3 decreased slightly from 46.03 to 41.82 emu/g after compounding the non-magnetic MoS_2. Nevertheless, the Co-γ-Fe_2O_3/MoS_2 still demonstrated excellent magnetic properties, and it could be easily separated from the

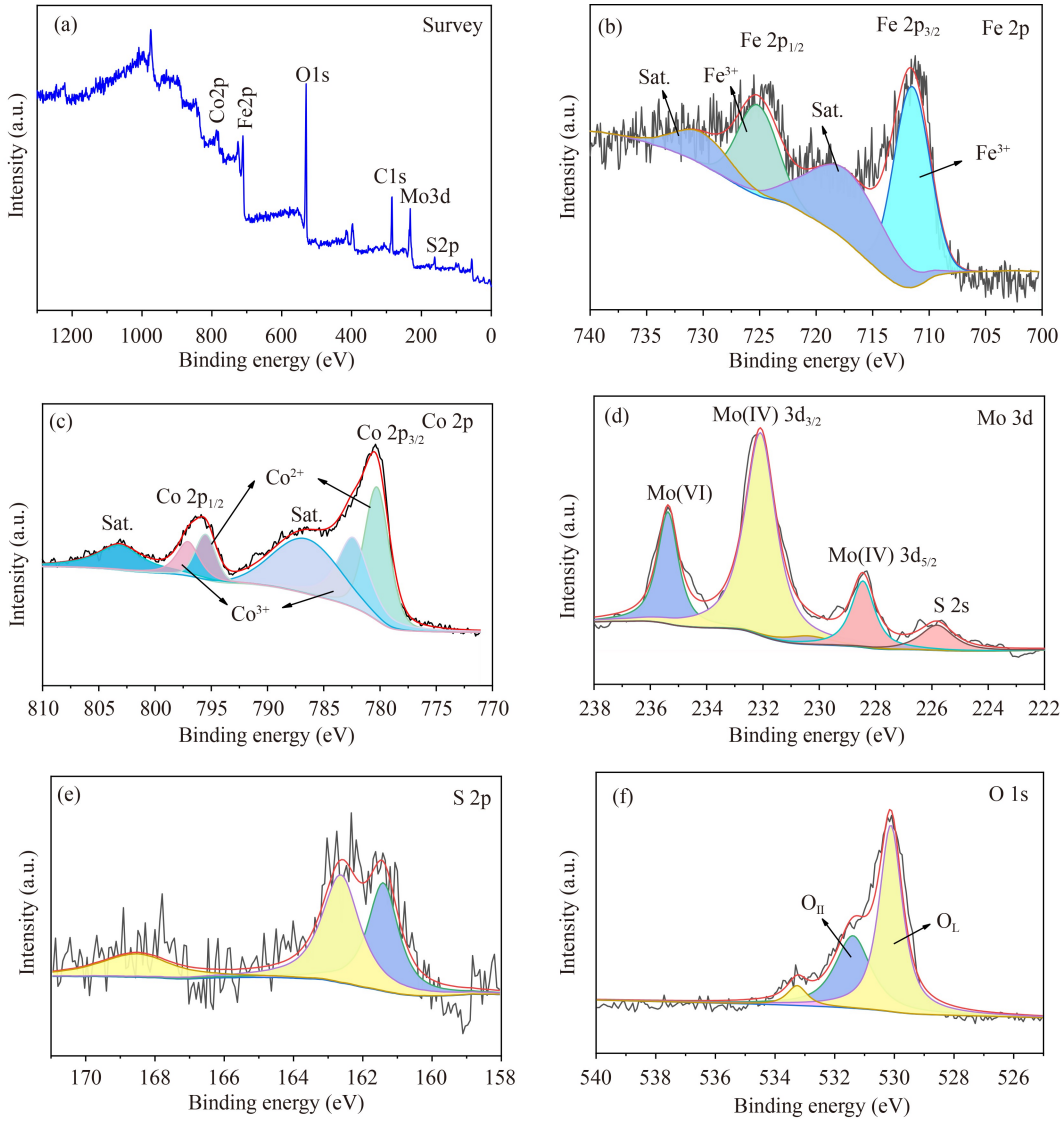

Fig. 2 (a) XPS survey, (b) Fe 2p, (c) Co 2p, (d) Mo 3d, (e) S 2p, and (f) O 1s XPS spectra of Co-γ-Fe_2O_3/MoS_2.

mixture by applying a magnetic field to rapidly recover Co-γ-Fe_2O_3/MoS_2.

3.2 Catalytic performance of synthesized catalysts

3.2.1 Influence of molar Mo/Fe ratio

The effect of varying the molar Mo/Fe ratio on PMS activation by the catalysts for BPA removal is presented in Fig. S6(a). Compared with Co-γ-Fe_2O_3/PMS (98.2%), a slight increase in the BPA degradation efficiency was observed when the molar Mo/Fe ratio was raised from 1% to 4% in Co-γ-Fe_2O_3/MoS_2 catalysts, resulting in BPA degradation of 85.0%, 89.7%, 93.9%, and 95.9% at 30 min, respectively. When the Mo/Fe ratio was further increased to 6%, BPA removal was significantly improved (91.8% for Mo/Fe (5%) and 99.3% for Mo/Fe (6%) within 10 min). When the Mo/Fe ratio exceeded 6%, MoS_2 doping did not further influence BPA removal (99.2% for Mo/Fe (7%) and 98.1% for Mo/Fe (8%)). In Fig. S6(b), $\ln C_0/C$ exhibited a linear relationship with t, which can be expressed by Eq. (1):

$$\ln C_0/C = K_{app}t, \quad (1)$$

where C_0, C, and K_{app} denote the initial concentration of BPA, the concentration of BPA after t min of reaction, and the pseudo-first-order rate constant, respectively. It could be observed that K_{app} remarkably increased from CFM_0 to CFM_6. However, when the proportion of MoS_2 continued to increase, K_{app} remained nearly constant or slightly decreased. The appropriate amount of MoS_2 improved the catalytic activity, and CFM_6 expressed the highest catalytic performance with a K_{app} of 0.4799 min^{-1}, which was 3.83 times higher than

that of CFM_0 (0.1253 min^{-1}). Overall, the degradation rate of BPA was accelerated as more active sites were available upon increasing the MoS_2 content. In addition, the total BPA degradation was enhanced by activating PMS and promoting Fe^{2+}/Fe^{3+} cycling when MoS_2 was introduced, which generated active species capable of adsorbing BPA (Bai et al., 2020). The results show that only the optimal ratio of Mo/Fe demonstrated a significant promoting effect. Hence, a molar Mo/Fe ratio of 6% was identified as the optimal ratio in this work.

3.2.2 Influence of different reaction systems

The degradation efficiency of BPA was assessed for different reaction systems. As indicated in Fig. 3(a), in the presence of only γ-Fe_2O_3, Co-γ-Fe_2O_3, or Co-γ-Fe_2O_3/MoS_2, 8.0%, 9.0%, and 6.4% of BPA was removed, respectively. The results implied that only a small amount of BPA could be removed by adsorption on the surface of the materials (Sheng et al., 2019; Sun et al., 2020a). In the presence of PMS alone, only a small amount of BPA was degraded due to the weak oxidation capacity of small amounts of PDS generated by PMS (Zhang et al., 2020). For the MoS_2/PMS and γ-Fe_2O_3/PMS catalyst systems, removal efficiencies of 15% and 60% BPA were achieved, respectively, because the transition metal ions activated PMS to produce ROSs, which accelerated the removal of BPA. However, the

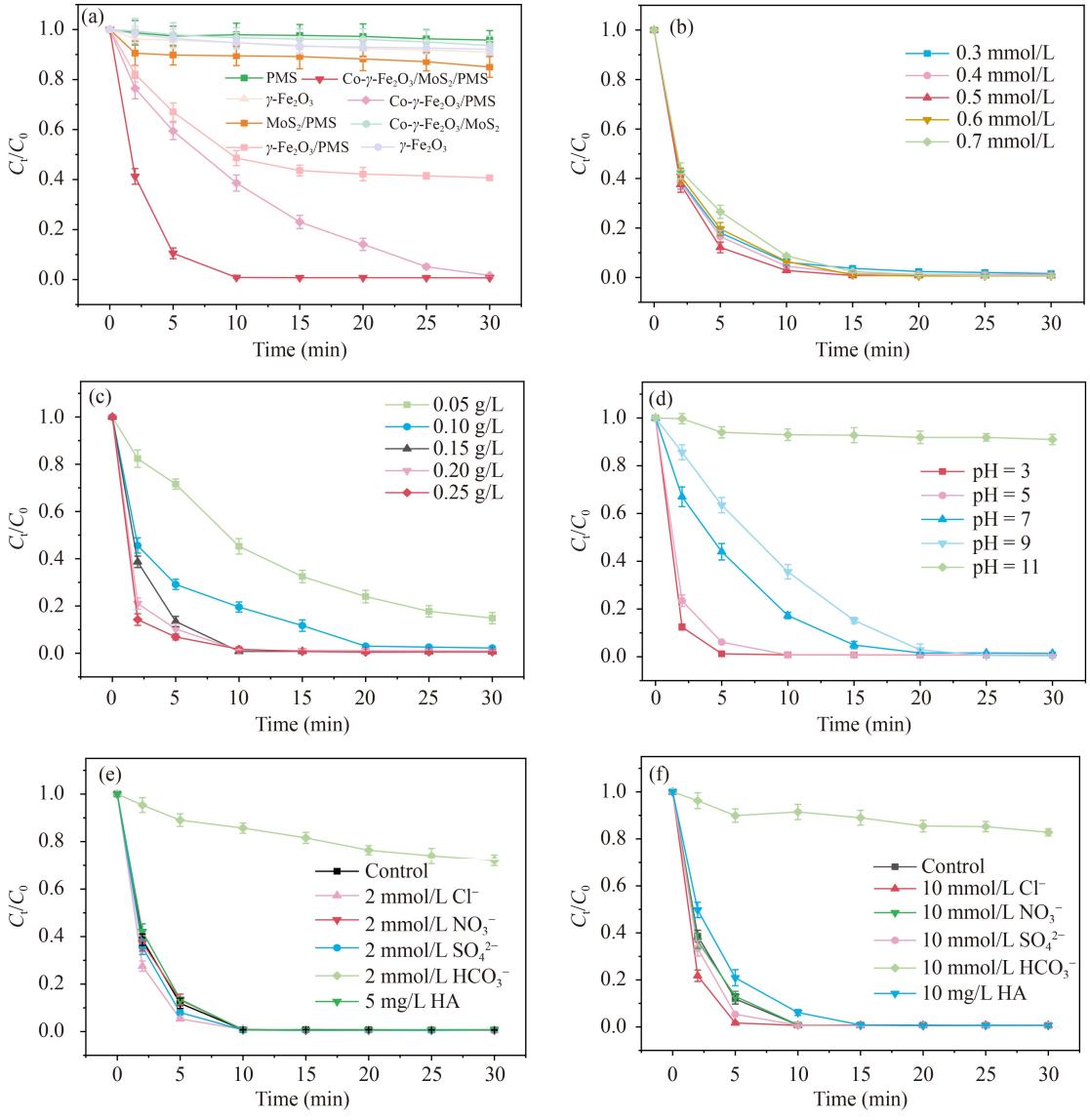

Fig. 3 (a) The removal efficiency of BPA under different reaction systems; the effects of (b) PMS concentration, (c) different catalyst dosages, (d) initial pH and (e, f) common anions (2, 10 mmol/L) and HA (5, 10 mg/L) on the removal of BPA; Experimental conditions: $[BPA]_0$ = 10 mg/L, $[Catalyst]_0$ = 0.15 g/L, $[PMS]_0$ = 0.5 mmol/L, pH_0 = 6.30.

decomposition of BPA was limited due to the low catalytic performance of MoS_2 and γ-Fe_2O_3. When using Co-γ-Fe_2O_3 and Co-γ-Fe_2O_3/MoS_2 as the heterogeneous catalysts, significant degradation of BPA was observed (Bai et al., 2020). Co-γ-Fe_2O_3 activated PMS to remove 98.3% of BPA in 30 min, while 99.3% of BPA could be removed by the Co-γ-Fe_2O_3/MoS_2/PMS system in 10 min. This demonstrated that Co doping dramatically improved the catalytic performance, and the decomposition rate was accelerated via compounding MoS_2. As evident from the data in Table S1, Co-γ-Fe_2O_3/MoS_2 exhibited excellent catalytic activity for PMS to degrade BPA in a shorter reaction time compared with previously reported catalysts.

3.2.3 Influence of different reaction conditions

Variations in the initial pH, PMS, and catalyst concentration are essential factors during catalytic oxidation. The effect of PMS concentration on the degradation of BPA via the Co-γ-Fe_2O_3/MoS_2/PMS system is displayed in Fig. 3(b). The efficiency of BPA removal gradually improved when the PMS concentration increased from 0.3 to 0.5 mmol/L, since higher PMS concentrations generated more ROSs (Li et al., 2020). However, the degradation efficiency slightly declined when the PMS concentration was further increased, which was attributed to several reasons: 1) PMS could not be fully activated due to the limited active sites of Co-γ-Fe_2O_3/MoS_2; 2) excess PMS might have reacted with free radicals (•OH, $SO_4^{\bullet-}$), as shown in Eqs. (2) and (3) (Bai et al., 2020).

$$HSO_5^- + SO_4^{\bullet-} \rightarrow SO_5^{\bullet-} + SO_4^{2-} + H^+ \quad (2)$$

$$HSO_5^- + \bullet OH \rightarrow SO_5^{\bullet-} + H_2O \quad (3)$$

As demonstrated in Fig. 3(c), there was a significant enhancement in the BPA removal efficiency from 84.0% to 99.1% when the amount of Co-γ-Fe_2O_3/MoS_2 was raised from 0.05 to 0.15 g/L. The removal efficiency remained almost constant upon further increasing it to 0.25 g/L, which implies that 0.15 g/L of catalyst provided enough active sites to activate PMS. Therefore, 0.15 g/L of Co-γ-Fe_2O_3/MoS_2 was used for subsequent experiments.

The influence of initial pH on BPA degradation was studied. In Fig. 3(d), the efficiency of BPA decomposition changed with initial pH. This impact of pH on BPA removal was caused by the formation of different active species. The first pK_a of BPA is 9.2 (Zhang et al., 2013), i.e., at pH values below 9.2, the cationic and zwitterionic molecular structures of BPA dominated, while the anionic form of BPA dominated above pH 9.2. Since the pK_a of PMS is 9.4, PMS mainly exists as HSO_5^- below pH 9.4 and is primarily composed of SO_5^{2-} at higher pH. Thus, at pH < 5.0, the combination of positive or neutral BPA molecules, negatively charged PMS, and positively charged catalyst surfaces promoted the removal of BPA. Simultaneously, due to the similar charge Co-γ-Fe_2O_3/MoS_2 and PMS, the decomposition efficiency of BPA was slightly reduced in the pH range of 5–9 (Sarkar et al., 2022b). Under highly alkaline conditions, $SO_4^{\bullet-}$ would be eliminated by hydroxyl ions to form •OH (Niu et al., 2022), and PMS would be deprotonated and produce $\bullet SO_5^{2-}$ with weak oxidizing ability (Yao et al., 2022). Thus, the efficiency of BPA removal was noticeably reduced in highly alkaline environments.

3.2.4 Influence of environmental factors

Inorganic ions including Cl^-, NO_3^-, HCO_3^-, and SO_4^{2-} as well as natural organics such as humic acid (HA) are commonly found in natural water and might affect the removal efficiency of BPA. Therefore, the effects of these representative substances on the efficiency of BPA removal were studied, as presented in Figs. 3(e) and 3(f). The BPA removal efficiency was significantly promoted when the Cl^- concentration ranged from 2 to 10 mmol/L. This could be attributed to the following reasons: 1) a series of reactions occurred between Cl^- and $SO_4^{\bullet-}$ in the Co-γ-Fe_2O_3/MoS_2/PMS system to form highly oxidizing chlorine species, such as $Cl^\bullet$ and $Cl_2^{\bullet-}$ (Zhu et al., 2022) (Eqs. (4)–(7)); 2) the direct reactions of Cl^- with PMS generated HOCl and Cl_2, which promoted the degradation of BPA (Giannakis et al., 2021) (Eqs. (8) and (9)). In the presence of SO_4^{2-}, the BPA removal efficiency was slightly promoted when increasing the concentration from 2 to 10 mmol/L. This was possibly because SO_4^{2-} targeted the π electrons of BPA and facilitated the breaking of bonds in the organic molecule, which decreased the energy barriers of $SO_4^{\bullet-}$ to attack BPA.

$$Cl^- + SO_4^{\bullet-} \rightarrow Cl^\bullet + SO_4^{2-} \quad (4)$$

$$Cl^- + \bullet OH \rightarrow HOCl^{\bullet-} \quad (5)$$

$$HOCl^{\bullet-} + H^+ \rightarrow Cl^\bullet + H_2O \quad (6)$$

$$Cl^- + Cl^\bullet \rightarrow Cl_2^{\bullet-} \quad (7)$$

$$Cl^- + HSO_5^- \rightarrow HOCl + SO_4^{2-} \quad (8)$$

$$Cl^- + HSO_5^- + H^+ \rightarrow SO_4^{2-} + Cl_2 + H_2O \quad (9)$$

Generally, NO_3^- in solution reacts with •OH and $SO_4^{\bullet-}$ to form the less-oxidizing $NO_3^\bullet$ (Eqs. (10) and (11)) but it suppresses the BPA removal efficiency only to a small extent, which could be basically ignored even at high concentrations (Niu et al., 2022).

$$SO_4^{\bullet-} + NO_3^- \rightarrow SO_4^{2-} + NO_3^\bullet \quad (10)$$

$$NO_3^- + \bullet OH \rightarrow NO_3^{\bullet} + OH^- \quad (11)$$

However, in the presence of HCO_3^-, the degradation of BPA was reduced, even at low concentrations (2 mmol/L). As an explanation for this strong effect, HCO_3^- reacted with H^+ to neutralize the environment, the marginal S atoms in MoS_2 were not easily trapped, and the activation of PMS by Mo(IV) was remarkably inhibited.

Natural organic matter (NOM) in the environment often competes with ROSs to decrease the removal efficiency of advanced oxidation processes for organic pollutants. The BPA removal percentage declined gradually as the concentration of HA increased from 5 to 10 mg/L because HA competed with BPA for the generated free radical species and reduced the number of active species in the reaction system. In addition, HA was adsorbed on the catalyst surface, covering the active sites to weaken interactions of the catalyst with PMS and BPA (Chen et al., 2018; Giannakis et al., 2021).

3.3 Mechanism of BPA degradation

3.3.1 Identification of major ROSs

To analyze the dominant ROSs generated in the Co-γ-Fe_2O_3/MoS_2/PMS system, MeOH, TBA, and *p*-BQ were added to the degradation system to quench various ROSs. The reaction rates of these quenching agents are $kSO_4^{\bullet-}$ = 2.5 × 10^7 $M^{-1}\cdot s^{-1}$ and $k_{\bullet OH}$ = 9.7 × 10^8 $M^{-1}\cdot s^{-1}$ for MeOH, k•OH = 3.8 × 10^8–7.6 × 10^8 $M^{-1}\cdot s^{-1}$ for TBA, and $kO_2^{\bullet-}$ = 3.5 × 10^8–7.8 × 10^8 $M^{-1}\cdot s^{-1}$ for *p*-BQ (Bai et al., 2020). As shown in Fig. 4(a), the BPA degradation efficiency was hardly affected by adding 25 mmol/L *p*-BQ (50 times the PMS concentration). When 250 mmol/L TBA (500 times the PMS concentration) was added, the removal of BPA was slightly inhibited, and its removal rate decreased to 94.1% in 30 min. Furthermore, the removal efficiency dropped sharply to 36.4% in the presence of 250 mmol/L MeOH (500 times the PMS concentration). The above results indicated that $SO_4^{\bullet-}$ played a major role in the reaction. To assess the possible involvement of $^1O_2$ as part of a non-radical decomposition pathway, furfuryl alcohol (FFA) was chosen as a quenching agent with reaction rates of 1.5 × 10^{10} $M^{-1}\cdot s^{-1}$ and 1.2 × 10^8 $M^{-1}\cdot s^{-1}$ for •OH and $^1O_2$ (Ren et al., 2022), respectively. Specifically, the addition of 10 mmol/L FFA (20 times the PMS concentration) remarkably inhibited BPA degradation, which was more pronounced than MeOH, indicating that the contribution of $^1O_2$ to BPA decomposition could not be overlooked.

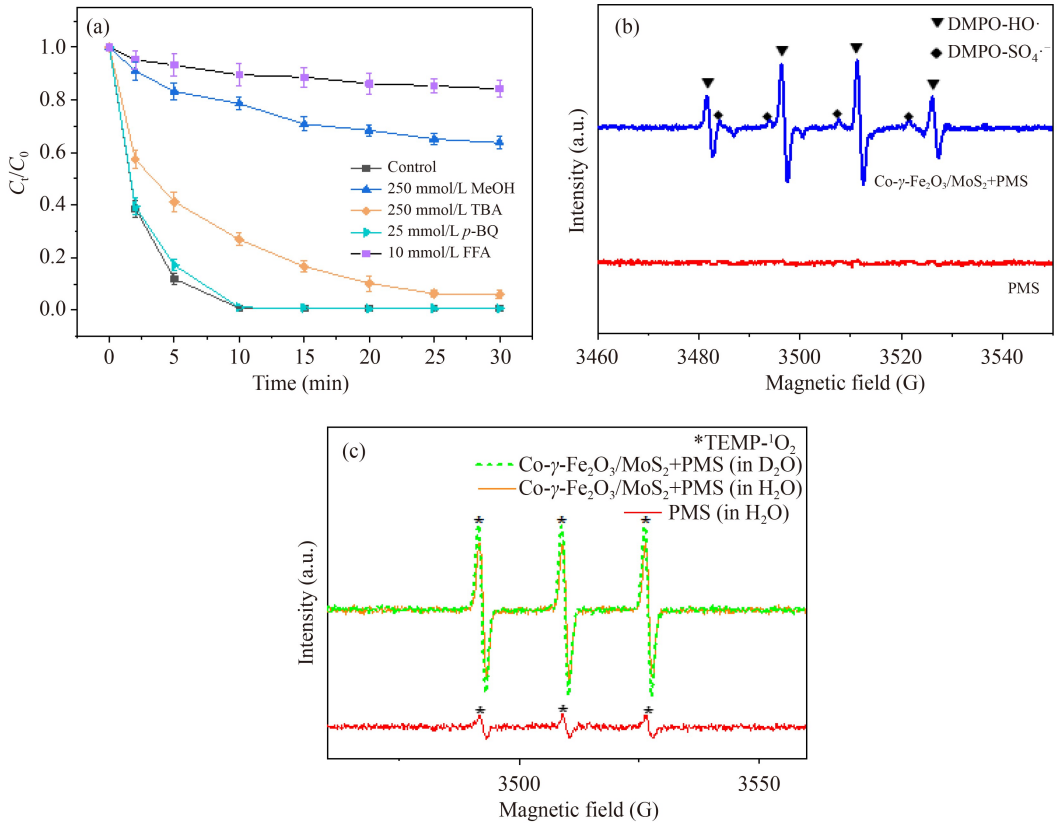

Fig. 4 (a) Effect of quenchers on BPA degradation in Co-γ-Fe_2O_3/MoS_2/PMS system; ESR spectra obtained using DMPO (b) and TEMP (c) as spin-trapping agent in H_2O- and D_2O-based. Experimental conditions: $[BPA]_0$ = 10 mg/L, $[Catalyst]_0$ = 0.15 g/L, $[PMS]_0$ = 0.5 mmol/L, pH_0 = 6.30.

To further determine the ROSs generated in the system, the EPR test was performed using DMPO and TEMP as spin-trapping agents. As displayed in Fig. 4(b), no signal of free radicals was observed in the pure PMS system because PMS could not be activated without a catalyst. In contrast, the typical signal of DMPO-•OH with a peak ratio of 1:2:2:1 was detected in the Co-γ-Fe_2O_3/MoS_2/PMS system, while some weak signals around these four peaks could be attributed to DMPO-$SO_4^{\bullet-}$. When TEMP was used instead of DMPO, a weak 1:1:1 triplet signal peak of $^1O_2$ could be discovered in the pure PMS system (Fig. 4(c)), which was the result of the autolysis of PMS, which would reasonably explain why BPA was slightly degraded in the pure PMS system (Sarkar et al., 2022b). The intensity of the TEMP-$^1O_2$ signal increased significantly with the addition of the catalyst, indicating that PMS produced a large amount of $^1O_2$ due to activation by the catalyst. To further examine the generation of $^1O_2$, we tested the singlet oxygen in D_2O by ESR because $^1O_2$ had a longer lifetime in D_2O (20–32 μs) (Yun et al., 2018). As demonstrated in Fig. 4(c), by comparing the typical triple ESR signal intensity of $^1O_2$ in both water bodies, the signal intensity in D_2O was stronger than that in H_2O. Previous experiments have demonstrated that singlet oxygen plays an important role in the BPA degradation process. Higher reaction kinetic constants are predicted for the degradation of BPA in D_2O than in H_2O (Chen et al., 2019a; Wu et al., 2020). The above results indicated that BPA could be degraded via both radical and non-radical pathways, where $^1O_2$ and $SO_4^{\bullet-}$ were the major ROSs.

3.3.2 Mechanistic analysis of Co-γ-Fe_2O_3/MoS_2/PMS system

The chemical surface compositions of fresh and used Co-γ-Fe_2O_3/MoS_2 were determined by XPS, as presented in Fig. 5. In the Fe 2p XPS spectra (Fig. 5(a)), the Fe $2p_{3/2}$ peak of used Co-γ-Fe_2O_3/MoS_2 was split into two peaks at 710.6 and 712.4 eV, relating to Fe^{2+} and Fe^{3+}, respectively. The Fe $2p_{1/2}$ peak was also split into two peaks at 724.1 eV (Fe^{2+}) and 726.3 eV (Fe^{3+}) (Niu et al., 2021), indicating that Fe^{3+} on the catalyst surface was partially reduced to Fe^{2+}. Correspondingly, the relative contents of different Co valence states varied slightly before and after the reaction (Fig. 5(b)), and a decrease in the amount of Co^{2+} from 54.4% to 51.1% was accompanied by an increase in Co^{3+} from 45.6% to 48.9%. The rather small change in the Co^{2+}/Co^{3+} ratio indicated that Co^{2+} was mostly regenerated after Co^{3+} reduction, allowing Co-γ-Fe_2O_3/MoS_2 to maintain an excellent activation potential (Fan et al., 2017). Furthermore, in Fig. 5(c), the Mo^{4+}/Mo^{6+} ratios on the surface of Co-γ-Fe_2O_3/MoS_2 before and after the reaction were 2.704 and 3.167, respectively. An increase in the amount of Mo^{4+} indicated that Mo^{4+} could be rapidly regenerated after the reaction, thus accelerating the rate of Fe^{2+}/Fe^{3+} cycling (Zeng et al., 2019a). Therefore, the content of Fe^{2+}, Co^{2+}, and Mo^{4+} all increased, which was favorable for the decomposition of BPA.

Based on the results discussed above and previous literature, possible mechanisms of PMS activation including both radical and non-radical pathways are presented in Fig. 6. First, Co^{3+} and/or Fe^{3+} were consumed by PMS to regenerate Co^{2+} and/or Fe^{2+}, while $SO_5^{\bullet-}$ with a lower activity was formed (Eq. (12)). Then, the HSO_5^- that originated from PMS was activated by Co^{2+} and/or Fe^{2+} to reduce to $SO_4^{\bullet-}$ (Eq. (13)) (Liu et al., 2021b). Since the standard redox potential of Co^{2+}/Co^{3+} (1.81 V) is higher than that of Fe^{2+}/Fe^{3+} (0.77 V), Co^{3+} could be reduced by Fe^{2+} (Eq. (14)). Secondly, $SO_5^{\bullet-}$ could be further converted to $^1O_2$ by reaction with H_2O (Eq. (15)) (Sun et al., 2020b). Furthermore, $^1O_2$ could also be generated by chemisorbed oxygen (O*) from lattice oxygen (O_{Lat}) in the presence of PMS (Eqs. (16) and (17)), while $SO_4^{\bullet-}$ could be hydrolyzed to produce •OH (Eq. (18)) (Dong et al., 2019). Mo^{4+} might be oxidized to Mo^{6+} by PMS, accompanied by the formation of $SO_4^{\bullet-}$ and •OH (Eq. (19)). After the removal of S atoms, the exposed Mo^{4+} became very reactive and contributed to the Fe^{3+}/Fe^{2+} cycle (Eq. (20)) (Zeng et al., 2019b). Finally, BPA would be removed and mineralized by large amounts of $^1O_2$, $SO_4^{\bullet-}$, and •OH (Eq. (21)).

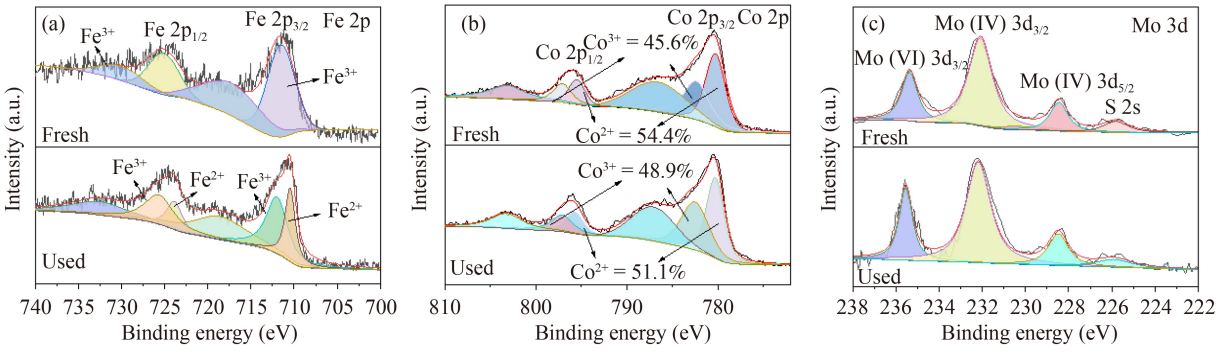

Fig. 5 (a) Fe 2p XPS spectra, (b) Co 2p XPS spectra, and (c) Mo 3d XPS spectra of the fresh and used Co-γ-Fe_2O_3/MoS_2.

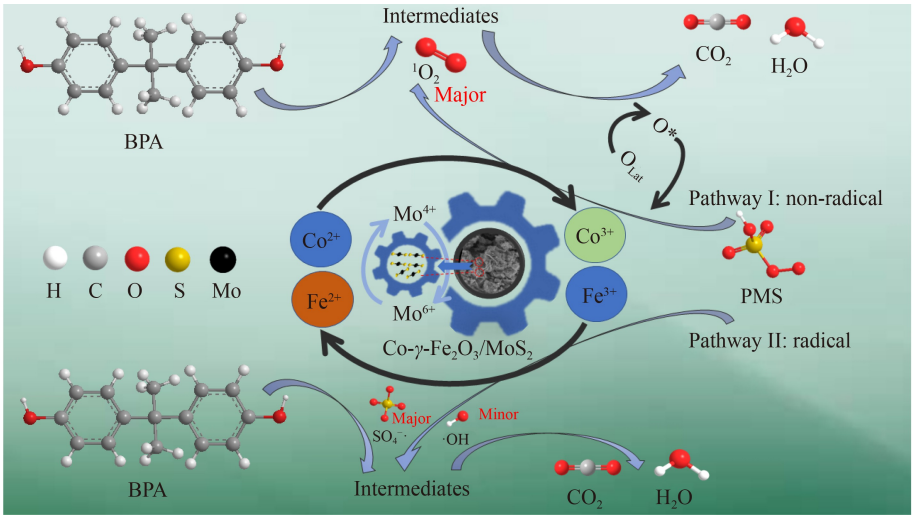

Fig. 6 Possible degradation mechanism of BPA in Co-γ-Fe_2O_3/MoS_2/PMS system.

$$Co^{3+}/Fe^{3+} + HSO_5^- \rightarrow Co^{2+}/Fe^{2+} + SO_5^{\cdot-} + H^+ \quad (12)$$

$$Co^{2+}/Fe^{2+} + HSO_5^- \rightarrow Co^{3+}/Fe^{3+} + SO_4^{\cdot-} + OH^- \quad (13)$$

$$Fe^{2+} + Co^{3+} \rightleftharpoons Fe^{3+} + Co^{2+} \quad (14)$$

$$2SO_5^{\cdot-} + H_2O \rightarrow 1.5\,^1O_2 + 2HSO_4^- \quad (15)$$

$$O_{Lat} \rightarrow O^* \quad (16)$$

$$HSO_5^- + O^* \rightarrow {}^1O_2 + HSO_4^- \quad (17)$$

$$SO_4^{\cdot-} + H_2O \rightarrow SO_4^{2-} + \cdot OH + H^+ \quad (18)$$

$$Mo^{4+} + HSO_5^- \rightarrow Mo^{6+} + SO_4^{\cdot-} + OH^- \quad (19)$$

$$Mo^{4+} + Fe^{3+} \rightarrow Mo^{6+} + Fe^{2+} \quad (20)$$

$$SO_4^{\cdot-} + {}^1O_2 + \cdot OH + BPA \rightarrow \text{Degradation products} \rightarrow CO_2 + H_2O \quad (21)$$

3.3.3 Possible degradation pathways of BPA

LC-MS was used to identify the intermediates in the Co-γ-Fe_2O_3/MoS_2 reaction system to explore the possible degradation pathways of BPA. Ten products (P1–P10) were formed mainly via oxidation, hydroxylation, and ring cleavage. The obtained mass spectra of the intermediates and the corresponding molecular formulae and different mass-to-charge (m/z) ratios are provided in Fig. S7 and Table S2. According to the products detected by LC-MS and previous studies, three possible decomposition pathways of BPA were formulated (Fig. 7). In the first possible route, the BPA molecule was hydroxylated to form P1 (Kakavandi et al., 2022) due to the attack of ROSs, after which P1 was deprotonated and dehydrated to open the ring to form P2. Then, P4 and P5 were formed after ring opening, hydroxylation, and oxidation of the benzene ring of P1 and P2 by ROS attack and finally further oxidized to P7. In pathway II, the BPA molecule was attacked by ROSs causing ring cleavage to form P3. The electron-rich C–C bond on P3 was broken due to the attack of its methyl group by the ROSs, followed by conversion to P6 (Wang et al., 2022a). Finally, the *para*-phenol P10 was generated due to oxidation and C–C bond fission of P6 (Yang et al., 2022). In another pathway, the dimer P8 was produced by the oxidation and polymerization of BPA, which was then further oxidized to P9. Eventually, the resulting intermediates were degraded to small-molecule products or mineralized to CO_2 and H_2O (Sun et al., 2020a; Liu et al., 2021b; Liu et al., 2022).

3.3.4 Toxicity analysis of intermediate products

The toxicity of BPA and its intermediates was predicted by quantitative structure-activity relationship (QSAR) using a toxicity estimation software tool (T.E.S.T.), as shown in Fig. 8. In Fig. 8(a), although most of the products were more mutagenic than BPA, all of them were negative, including P3, P4, and P5, which had positive mutagenicity, which became negative after being attacked by ROSs (Jiang et al., 2020). In addition, all the products except P2, P8, and P9 were less developmentally toxic than BPA (Fig. 8(b)). Interestingly, Fig. 8(c) reveals that the bioconcentration factors of the intermediate products were smaller than those of BPA except for P1, P6, P7, P8, and P9. They were further reduced due to hydroxylation reactions, diminishing their threat to the environment (Yang et al., 2021). In addition, the acute toxicity of BPA and its intermediates was evaluated by fathead minnow LC_{50} (96 h) (i.e., the compound concentration that killed 50% of fathead minnow after

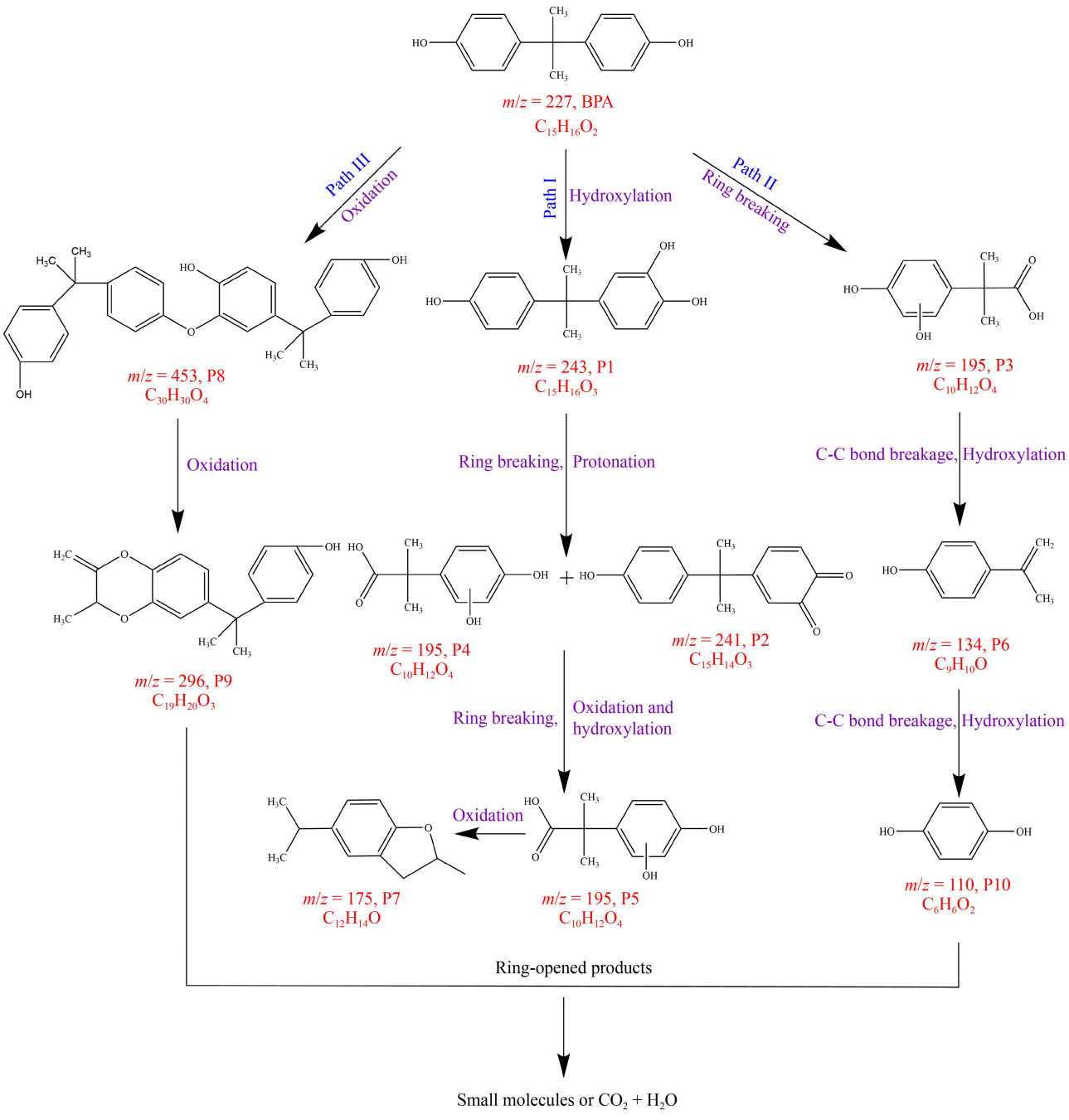

Fig. 7 Proposed degradation pathways of BPA in the Co-γ-Fe_2O_3/MoS_2/PMS system.

96 h), and the results are displayed in Fig. 8(d), where the acute toxicity of all products was lower than that of BPA except for P1, P7, P8, and P9. Overall, the overall toxicity of BPA and its intermediates was reduced after degradation in the Co-γ-Fe_2O_3/MoS_2/PMS system.

3.4 Evaluation of catalyst applicability

To investigate the degradation ability of Co-γ-Fe_2O_3/MoS_2 toward other representative organic pollutants, levofloxacin (LFX), sulfamethoxazole (SMX), carbamazepine (CBZ), tetracycline (TC), and ciprofloxacin (CIP) were studied as contaminants. The experimental conditions were consistent with the conditions for BPA degradation, and the results are shown in Fig. S8. According to Fig. S8(a), the removal rates of the selected pollutants by the Co-γ-Fe_2O_3/MoS_2/PMS system all exceeded 80%, and their corresponding reaction rate constants well all high, with the largest value corresponding to BPA (0.4799 min^{-1})

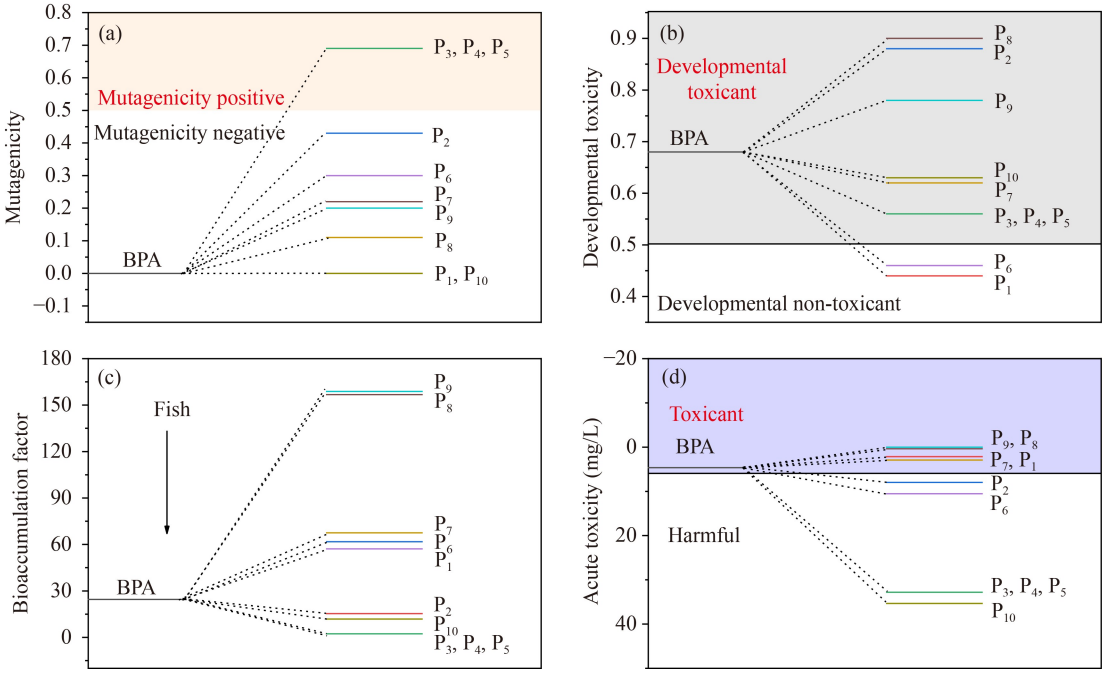

Fig. 8 (a) mutagenicity, (b) developmental toxicity, (c) bioaccumulation factor, and (d) acute toxicity of BPA and its degradation intermediates.

and a relatively slow reaction rate for TC (0.0751 min^{-1}) (Fig. S8(b)). The lower TC removal efficiency and corresponding reaction rate constant may be related to its relatively large molecular weight (He et al., 2022a), which decreased the removal efficiency. Thus, TC may require a large amount of PMS to be effectively degraded.

The reusability of catalysts is indispensable for practical applications. To examine the reusability of Co-γ-Fe_2O_3 and Co-γ-Fe_2O_3/MoS_2, cycling experiments were performed to remove BPA. As demonstrated in Fig. 9(a), the speed of BPA removal by Co-γ-Fe_2O_3 was significantly reduced in the fourth and fifth cycles. This might be explained by the damage of the active sites of Co-γ-Fe_2O_3 caused by the intermediate products of BPA during the removal process and the adsorption of SO_4^{2-} and organic pollutants on the surface of Co-γ-Fe_2O_3 (Zheng et al., 2019). Additionally, the XRD patterns of Co-γ-Fe_2O_3 before use and after the fifth cycle (Fig. 9(b)) revealed the disappearance of the diffraction peak corresponding to the (111) crystal plane, indicating the poor stability of Co-γ-Fe_2O_3. The results of the cycling experiment after compounding MoS_2 are shown in Fig. 9(c). After five cycles, the removal of BPA still exceeded 99%. In addition, the comparison of XRD patterns and the XPS and VSM results before and after the reaction indicated that the structural stability of Co-γ-Fe_2O_3 was enhanced after MoS_2 compounding (He et al., 2022a). Furthermore, in the Co-γ-Fe_2O_3/PMS system, the leached contents of Fe ions and Co ions after the reaction were 6.983 and 0.697 mg/L, respectively. However, they were only 1.904 and 0.201 mg/L in the Co-γ-Fe_2O_3/MoS_2/PMS system (Fig. S9), which could be assigned to the synergistic effect between Fe, Co, and Mo (Sun et al., 2020b).

4 Conclusions

The environmentally friendly magnetic Co-γ-Fe_2O_3/MoS_2 nanocomposite was synthesized by a two-step hydrothermal method through *in situ* growth of MoS_2 nanosheets on Co-γ-Fe_2O_3 nanoparticles. The Co-γ-Fe_2O_3/MoS_2/PMS system exhibited an excellent BPA removal efficiency due to the synergistic effect between Fe, Co, and Mo. In the Co-γ-Fe_2O_3/MoS_2/PMS system, the BPA removal rate remained above 99% within 30 min after five reuse cycles of the catalyst. Its ability to maintain a high efficiency indicated that Co-γ-Fe_2O_3 possessed excellent stability and low ion leaching after compounding with MoS_2. In addition, both radicals and non-radicals were involved in the degradation of BPA, and $^1O_2$ and $SO_4^{\bullet-}$ were the main ROSs in the Co-γ-Fe_2O_3/MoS_2/PMS system. Ten intermediates of BPA degradation were identified by LC-MS, and three possible decomposition pathways were proposed. The toxicities of BPA and its intermediates were predicted by T.E.S.T, indicating that the toxicity of BPA was reduced after degradation by the Co-γ-Fe_2O_3/MoS_2/PMS system, which demonstrated its potential applications for degrading BPA in actual water bodies. Overall, Co-γ-Fe_2O_3/MoS_2 is an efficient and durable catalyst with wide applicability and a promising future for organic pollutant treatment.

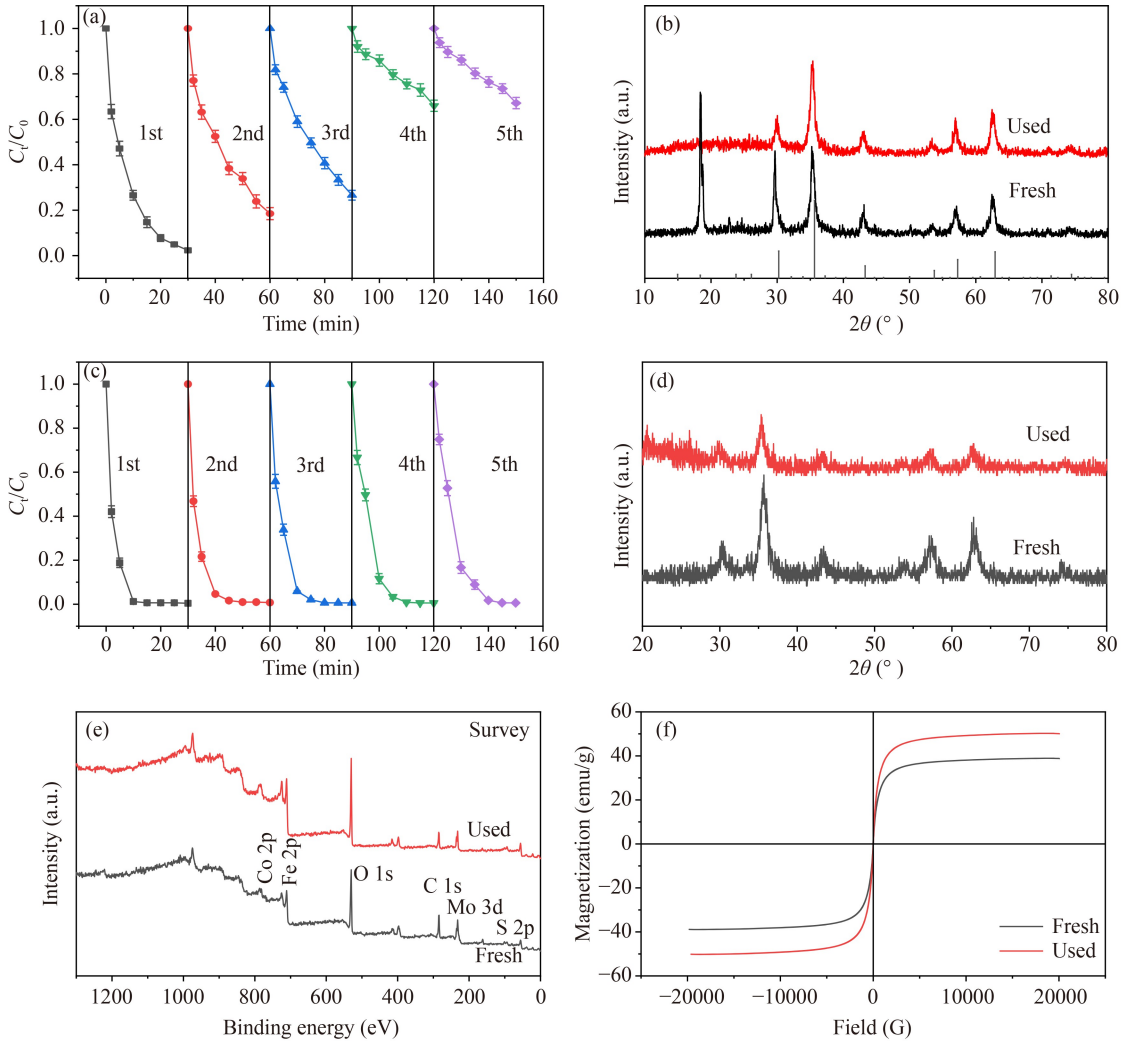

Fig. 9 (a) Cycling test of Co-γ-Fe_2O_3 for the degradation of BPA; (b) XRD patterns of Co-γ-Fe_2O_3 before and after the reaction; (c) stability of Co-γ-Fe_2O_3/MoS_2 for the degradation of BPA; (d) XRD patterns, (e) XPS survey patterns, and (f) magnetic hysteresis loops of fresh and used Co-γ-Fe_2O_3/MoS_2.

Acknowledgements This work was financially supported by Natural Science Foundation of Fujian Province (China) (No. 2022J0113) and Fuzhou University Testing Fund of Precious Apparatus (China) (No. 2022T025)

Declaration of Competing Interest The authors declare that this manuscript has been prepared with the consent of all authors and without financial conflict of interest.

Electronic Supplementary Material Supplementary material is available in the online version of this article at https://doi.org/10.1007/s11783-024-1797-2 and is accessible for authorized users.

Funding Note Open access funding provided by Technical University of Denmark.

References

Abareshi A, Salehi N (2022). The effect of Fe_3O_4 nanoparticles on structural, optical, and thermal properties MoS_2 nanoflakes. Journal of Materials Science Materials in Electronics, 33(33): 25153–25162

Bai R, Yan W, Xiao Y, Wang S, Tian X, Li J, Xiao X, Lu X, Zhao F (2020). Acceleration of peroxymonosulfate decomposition by a magnetic MoS_2/$CuFe_2O_4$ heterogeneous catalyst for rapid degradation of fluoxetine. Chemical Engineering Journal, 397: 125501

Barik R, Jena B K, Mohapatra M (2017). Metal doped mesoporous

FeOOH nanorods for high performance supercapacitors. RSC Advances, 7(77): 49083–49090

Chen C, Ma T, Shang Y, Gao B, Jin B, Dan H, Li Q, Yue Q, Li Y, Wang Y, et al. (2019a). *In-situ* pyrolysis of enteromorpha as carbocatalyst for catalytic removal of organic contaminants: considering the intrinsic N/Fe in enteromorpha and non-radical reaction. Applied Catalysis B: Environmental, 250: 382–395

Chen G, Zhang X, Gao Y, Zhu G, Cheng Q, Cheng X (2019b). Novel magnetic MnO_2/$MnFe_2O_4$ nanocomposite as a heterogeneous catalyst for activation of peroxymonosulfate (PMS) toward oxidation of organic pollutants. Separation and Purification Technology, 213: 456–464

Chen L, Ding D, Liu C, Cai H, Qu Y, Yang S, Gao Y, Cai T (2018). Degradation of norfloxacin by $CoFe_2O_4$-GO composite coupled with peroxymonosulfate: a comparative study and mechanistic consideration. Chemical Engineering Journal, 334: 273–284

Dong H, Chen J, Feng L, Zhang W, Guan X, Strathmann T J (2019). Degradation of organic contaminants through activating bisulfite by cerium(IV): a sulfate radical-predominant oxidation process. Chemical Engineering Journal, 357: 328–336

Duan X, Su C, Miao J, Zhong Y, Shao Z, Wang S, Sun H (2018). Insights into perovskite-catalyzed peroxymonosulfate activation: maneuverable cobalt sites for promoted evolution of sulfate radicals. Applied Catalysis B: Environmental, 220: 626–634

Fan Y, Ji Y, Zheng G, Lu J, Kong D, Yin X, Zhou Q (2017). Degradation of atrazine in heterogeneous Co_3O_4 activated peroxymonosulfate oxidation process: kinetics, mechanisms, and reaction pathways. Chemical Engineering Journal, 330: 831–839

Flak D, Chen Q, Mun B S, Liu Z, Rękas M, Braun A (2018). *In situ* ambient pressure XPS observation of surface chemistry and electronic structure of α-Fe_2O_3 and γ-Fe_2O_3 nanoparticles. Applied Surface Science, 455: 1019–1028

Gao J, Song J, Ye J, Duan X, Dionysiou D D, Yadav J S, Nadagouda M N, Yang L, Luo S (2021). Comparative toxicity reduction potential of UV/sodium percarbonate and UV/hydrogen peroxide treatments for bisphenol A in water: an integrated analysis using chemical, computational, biological, and metabolomic approaches. Water Research, 190: 116755

Ge Y, Li C, Waterhouse G I N, Jiang X, Zhang Z, Yu L (2021). Polypyrrole/γ-Fe_2O_3/g-C_3N_4 nanocomposites for high-performance electromagnetic wave absorption. Synthetic Metals, 274: 116716

Geng Y, Chen D, Li N, Xu Q, Li H, He J, Lu J (2021). Z-scheme 2D/2D α-Fe_2O_3/g-C_3N_4 heterojunction for photocatalytic oxidation of nitric oxide. Applied Catalysis B: Environmental, 280: 119409

Giannakis S, Lin K A, Ghanbari F (2021). A review of the recent advances on the treatment of industrial wastewaters by sulfate radical-based advanced oxidation processes (SR-AOPs). Chemical Engineering Journal, 406: 127083

Golestani E, Javanbakht M, Ghafarian-Zahmatkesh H, Beydaghi H, Ghaemi M (2018). Tartaric acid assisted carbonization of $LiFePO_4$ synthesized through *in situ* hydrothermal process in aqueous glycerol solution. Electrochimica Acta, 259: 903–915

Guo P, Hu X (2022). Co, Fe co-doped g-C_3N_4 composites as peroxymonosulfate activators under visible light irradiation for levofloxacin degradation: characterization, performance and synergy mechanism. Colloids and Surfaces. A, Physicochemical and Engineering Aspects, 648: 129423

He Y, Qian J, Wang P, Wu J, Lu B, Tang S, Gao P (2022a). Acceleration of levofloxacin degradation by combination of multiple free radicals via MoS_2 anchored in manganese ferrite doped perovskite activated PMS under visible light. Chemical Engineering Journal, 431: 133933

He Y, Qian J, Xu B, Wang P, Lu B, Tang S, Gao P (2022b). Encapsulate $SrCoO_3$ perovskite crystal within molybdenum disulfide layer as core-shell structure to enhance electron transfer for peroxymonosulfate activation. Separation and Purification Technology, 283: 120199

Ikram M, Khan M I, Raza A, Imran M, Ul-Hamid A, Ali S (2020). Outstanding performance of silver-decorated MoS_2 nanopetals used as nanocatalyst for synthetic dye degradation. Physica E, Low-Dimensional Systems and Nanostructures, 124: 114246

Jiang J, Wang X, Liu Y, Ma Y, Li T, Lin Y, Xie T, Dong S (2020). Photo-Fenton degradation of emerging pollutants over Fe-POM nanoparticle/porous and ultrathin g-C_3N_4 nanosheet with rich nitrogen defect: degradation mechanism, pathways, and products toxicity assessment. Applied Catalysis B: Environmental, 278: 119349

Kakavandi B, Alavi S, Ghanbari F, Ahmadi M (2022). Bisphenol A degradation by peroxymonosulfate photo-activation coupled with carbon-based cobalt ferrite nanocomposite: Performance, upgrading synergy and mechanistic pathway. Chemosphere, 287: 132024

Li J, Li J, Chen L, Lin Y, Liu X, Gong X, Li D (2015). Characterization and magnetism of Co-modified γ-Fe_2O_3 core-shell nanoparticles by enhancement using NaOH. Journal of Magnetism and Magnetic Materials, 374: 157–163

Li M, Li Y, Yu P, Zhao H, Xiang L, Feng N, Li Q, He K, Luo X, Cai Q, et al. (2022a). Exploring degradation mechanism of tetracycline via high-effective peroxymonosulfate catalysts of montmorillonite hybridized CoFe composites and safety assessment. Chemical Engineering Journal, 427: 130930

Li Q, Lv C, Xia X, Peng C, Yang Y, Guo F, Zhang J (2022b). Separation/degradation behavior and mechanism for cationic/anionic dyes by Ag-functionalized Fe_3O_4-PDA core-shell adsorbents. Frontiers of Environmental Science & Engineering, 16(11): 138

Li R, Huang J, Cai M, Huang J, Xie Z, Zhang Q, Liu Y, Liu H, Lv W, Liu G (2020). Activation of peroxymonosulfate by Fe doped g-C_3N_4/graphene under visible light irradiation for Trimethoprim degradation. Journal of Hazardous Materials, 384: 121435

Liu H, Luo S, Yan S, Wang Q, Hu D, Wang Y, Feng J, Yi T (2019). High-performance α-Fe_2O_3/C composite anodes for lithium-ion batteries synthesized by hydrothermal carbonization glucose method used pickled iron oxide red as raw material. Composites. Part B, Engineering, 164: 576–582

Liu L, Hu T, Dai K, Zhang J, Liang C (2021a). A novel step-scheme $BiVO_4$/Ag_3VO_4 photocatalyst for enhanced photocatalytic degradation activity under visible light irradiation. Chinese Journal of Catalysis, 42(1): 46–55

Liu M, Zhang L, Han L, Mei C, Xu C, Yuan R, Geng C (2023). Can heat-activated peroxymonosulfate be used as a pretreatment to mitigate fouling for membrane distillation: performance of individual organics? Water, 15(6): 1148

Liu T, Wang C, Han Y, Bai C, Ren H, Liu Y, Han X (2022). Oxidative polymerization of bisphenol A (BPA) via H-abstraction by $Bi_{2.15}WO_6$ and persulfate: importance of the surface complexes. Chemical Engineering Journal, 435: 134816

Liu Z, Wan J, Ma Y, Wang Y (2021b). *In situ* synthesis of FeOCl@MoS_2 on graphite felt as novel electro-fenton cathode for efficient degradation of antibiotic ciprofloxacin at mild pH. Chemosphere, 273: 129747

Long X, Luo J, Zhong Z, Zhu Y, Zhang C, Wan J, Zhou H, Zhang B, Xia D (2023). Performance and mechanism of carbamazepine removal by FeS-$S_2O_8^{2-}$ process: experimental investigation and DFT calculations. Frontiers of Environmental Science & Engineering, 17(9): 113

Lu J, Zhou Y, Ling L, Zhou Y (2022). Enhanced activation of PMS by a novel Fenton-like composite Fe_3O_4/S-WO_3 for rapid chloroxylenol degradation. Chemical Engineering Journal, 446: 137067

Lu Y, Ding Z, Zhang J, Fu C, Xia X, Fang Y (2019). Degradation of atrazine by UV/PMS in phosphate buffer. Polish Journal of Environmental Studies, 28(4): 2735–2744

Luciano A J R, de Sousa Soletti L, Ferreira M E C, Cusioli L F, de Andrade M B, Bergamasco R, Yamaguchi N U (2020). Manganese ferrite dispersed over graphene sand composite for methylene blue photocatalytic degradation. Journal of Environmental Chemical Engineering, 8(5): 104191

Ma Q, Zhang X, Guo R, Zhang H, Cheng Q, Xie M, Cheng X (2019). Persulfate activation by magnetic γ-Fe_2O_3/Mn_3O_4 nanocomposites for degradation of organic pollutants. Separation and Purification Technology, 210: 335–342

Mao J, Quan X, Wang J, Gao C, Chen S, Yu H, Zhang Y (2018). Enhanced heterogeneous Fenton-like activity by Cu-doped $BiFeO_3$ perovskite for degradation of organic pollutants. Frontiers of Environmental Science & Engineering, 12(6): 10

Niu B, Wang L, Li M, Yao W, Zang K, Zhou L, Hu X, Zheng Y (2022). Lattice B-doping evolved ferromagnetic perovskite-like catalyst for enhancing persulfate-based degradation of norfloxacin. Journal of Hazardous Materials, 425: 127949

Niu L, Zhang G, Xian G, Ren Z, Wei T, Li Q, Zhang Y, Zou Z (2021). Tetracycline degradation by persulfate activated with magnetic *γ*-Fe_2O_3/CeO_2 catalyst: performance, activation mechanism and degradation pathway. Separation and Purification Technology, 259: 118156

Pan X, Yan L, Qu R, Wang Z (2018). Degradation of the UV-filter benzophenone-3 in aqueous solution using persulfate activated by heat, metal ions and light. Chemosphere, 196: 95–104

Qi K, Yuan Z, Hou Y, Zhao R, Zhang B (2019). Facile synthesis and improved Li-storage performance of Fe-doped MoS_2/reduced graphene oxide as anode materials. Applied Surface Science, 483: 688–695

Ren W, Cheng C, Shao P, Luo X, Zhang H, Wang S, Duan X (2022). Origins of electron-transfer regime in persulfate-based nonradical oxidation processes. Environmental Science & Technology, 56(1): 78–97

Sakthi Athithan A S, Jeyasundari J, Jacob Y B A (2021). Biological synthesis, physico-chemical characterization of undoped and Co doped *α*-Fe_2O_3 nanoparticles using *Tribulus terrestris* leaf extract and its antidiabetic, antimicrobial applications. Advances in Natural Sciences. Nanoscience and Nanotechnology, 12(4): 045003

Sarkar P, De S, Neogi S (2022a). Microwave assisted facile fabrication of dual Z-scheme *g*-C_3N_4 /$ZnFe_2O_4$/Bi_2S_3 photocatalyst for peroxymonosulphate mediated degradation of 2,4,6-trichlorophenol: the mechanistic insights. Applied Catalysis B: Environmental, 307: 121165

Sarkar P, Roy D, Bera B, De S, Neogi S (2022b). Efficient photocatalytic degradation of ciprofloxacin using novel dual Z-scheme gCN/$CuFe_2O_4$/MoS_2 mediated peroxymonosulphate activation. Chemical Engineering Journal, 430: 132834

Sheng B, Yang F, Wang Y, Wang Z, Li Q, Guo Y, Lou X, Liu J (2019). Pivotal roles of MoS_2 in boosting catalytic degradation of aqueous organic pollutants by Fe(II)/PMS. Chemical Engineering Journal, 375: 121989

Su M, Li H, Liu Z, Peng H, Huang S, Zhou Y, Liao C, Song G, Chen D (2022). Highly-efficient and easy separation of *γ*-Fe_2O_3 selectively adsorbs U(VI) in waters. Environmental Research, 210: 112917

Sun Q, Xu B, Yang J, Qian T, Jiang H (2020a). Layered oxides supported Co–Fe bimetal catalyst for carbamazepine degradation via the catalytic activation of peroxymonosulfate. Chemical Engineering Journal, 400: 125899

Sun X, Xu D, Dai P, Liu X, Tan F, Guo Q (2020b). Efficient degradation of methyl orange in water via both radical and non-radical pathways using Fe–Co bimetal-doped MCM-41 as peroxymonosulfate activator. Chemical Engineering Journal, 402: 125881

Sun Z, Zhu Y, Deng Y, Liu F, Ruan W, Xie L, Beadham I (2022). Nature of surface active centers in activation of peroxydisulfate by CuO for degradation of BPA with non-radical pathway. Colloids and Surfaces. A, Physicochemical and Engineering Aspects, 643: 128731

Wang F, Lai Y, Fang Q, Li Z, Ou P, Wu P, Duan Y, Chen Z, Li S, Zhang Y (2020). Facile fabricate of novel Co(OH)F@MXenes catalysts and their catalytic activity on bisphenol A by peroxymonosulfate activation: the reaction kinetics and mechanism. Applied Catalysis B: Environmental, 262: 118099

Wang J, Xie Y, Hou J, Zhou X, Chen J, Yao C, Zhang Y, Li Y (2022a). Biodegradation of bisphenol A by alginate immobilized phanerochaete chrysosporium beads: continuous cyclic treatment and degradation pathway analysis. Biochemical Engineering Journal, 177: 108212

Wang Y, Wu L, Zhou Y, Zhang Y, Sun S, Duo Wu W, Wang X, Wu Z (2022b). Ternary FeS/*γ*-Fe_2O_3@N/S-doped carbon nanohybrids dispersed in an ordered mesoporous silica for efficient peroxymonosulfate activation. Chemical Engineering Journal, 435: 135124

Wang Z, Yang B, Zhao X, Chen Y, Wei D, Zhang L, Su X (2022c). Facile synthesis of ultrathin *γ*-Fe_2O_3 magnetic nanosheets rich in oxygen vacancies and their photocatalytic activity for water oxidation. Applied Surface Science, 578: 151999

Wu S, Liu H, Yang C, Li X, Lin Y, Yin K, Sun J, Teng Q, Du C, Zhong Y (2020). High-performance porous carbon catalysts doped by iron and nitrogen for degradation of bisphenol F via peroxymonosulfate activation. Chemical Engineering Journal, 392: 123683

Wu S, Yang Z, Wang F, Jin X, Kengara F, Xi K, Fang W, Yang W, Zhang Y (2022). Effect of γ-Fe_2O_3 nanoparticles on the composition of montmorillonite and its sorption capacity for pyrene. Science of the Total Environment, 813: 151893

Xie X, Cao J, Xiang Y, Xie R, Suo Z, Ao Z, Yang X, Huang H (2022). Accelerated iron cycle inducing molecular oxygen activation for deep oxidation of aromatic VOCs in MoS_2 co-catalytic Fe^{3+}/PMS system. Applied Catalysis B: Environmental, 309: 121235

Xu B, Wang J, Yu H, Gao H (2011). Large-scale synthesis of hierarchical flowerlike boehmite architectures. Journal of Environmental Sciences (China), 23(Suppl): S49–S52

Xu L, Wang X, Sun Y, Gong H, Guo M, Zhang X, Meng L, Gan L (2020). Mechanistic study on the combination of ultrasound and peroxymonosulfate for the decomposition of endocrine disrupting compounds. Ultrasonics Sonochemistry, 60: 104749

Yan T, Yang Q, Feng R, Ren X, Zhao Y, Sun M, Yan L, Wei Q (2022). Highly effective visible-photocatalytic hydrogen evolution and simultaneous organic pollutant degradation over an urchin-like oxygen-doped MoS_2/$ZnIn_2S_4$ composite. Frontiers of Environmental Science & Engineering, 16(10): 131

Yang G, Liang Y, Xiong Z, Yang J, Wang K, Zeng Z (2021). Molten salt-assisted synthesis of Ce_4O_7/Bi_4MoO_9 heterojunction photocatalysts for photo-fenton degradation of Tetracycline: enhanced mechanism, degradation pathway and products toxicity assessment. Chemical Engineering Journal, 425: 130689

Yang J, Zeng D, Hassan M, Ma Z, Dong L, Xie Y, He Y (2022). Efficient degradation of bisphenol A by dielectric barrier discharge non-thermal plasma: performance, degradation pathways and mechanistic consideration. Chemosphere, 286: 131627

Yao L, He X, Lv J, Xu G, Bao Z, Cui J, Yu D, Wu Y (2022). Efficient degradation of ciprofloxacin by Co_3O_4/Si nanoarrays heterojunction activated peroxymonosulfate under simulated sunlight: performance and mechanism. Journal of Environmental Chemical Engineering, 10(3): 107397

Yue Y, Shen S, Cheng W, Han G, Wu Q, Jiang J (2022). Construction of mechanically robust and recyclable photocatalytic hydrogel based on nanocellulose-supported CdS/MoS_2/montmorillonite hybrid for antibiotic degradation. Colloids and Surfaces. A, Physicochemical and Engineering Aspects, 636: 128035

Yun E, Lee J H, Kim J, Park H, Lee J (2018). Identifying the nonradical mechanism in the peroxymonosulfate activation process: singlet oxygenation versus mediated electron transfer. Environmental Science & Technology, 52(12): 7032–7042

Zeng L, Xiao L, Shi X, Wei M, Cao J, Long Y (2019a). Core-shell prussian blue analogues@ poly(m-phenylenediamine) as efficient peroxymonosulfate activators for degradation of rhodamine B with reduced metal leaching. Journal of Colloid and Interface Science, 534: 586–594

Zeng Y, Guo N, Song Y, Zhao Y, Li H, Xu X, Qiu J, Yu H (2018). Fabrication of Z-scheme magnetic MoS_2/$CoFe_2O_4$ nanocomposites with highly efficient photocatalytic activity. Journal of Colloid and Interface Science, 514: 664–674

Zeng Y, Guo N, Xu X, Yu Y, Wang Q, Wang N, Han X, Yu H (2019b). Degradation of bisphenol A using peroxymonosulfate activated by WO_3@MoS_2/Ag hollow nanotubes photocatalyst. Chemosphere, 227: 589–597

Zhang D, Fan X, Yang A, Zong X (2018). Hierarchical assembly of urchin-like alpha-iron oxide hollow microspheres and molybdenum disulphide nanosheets for ethanol gas sensing. Journal of Colloid and Interface Science, 523: 217–225

Zhang H, Du L, Xing J, Wei G, Quan X (2023). Electro-conductive crosslinked polyaniline/carbon nanotube nanofiltration membrane for electro-enhanced removal of bisphenol A. Frontiers of Environmental Science & Engineering, 17(5): 59

Zhang J, Sun B, Guan X (2013). Oxidative removal of bisphenol A by permanganate: kinetics, pathways and influences of co-existing chemicals. Separation and Purification Technology, 107: 48–53

Zhang W, Zhang H, Yan X, Zhang M, Luo R, Qi J, Sun X, Shen J, Han W, Wang L, et al. (2020). Controlled synthesis of bimetallic Prussian blue analogues to activate peroxymonosulfate for efficient bisphenol A degradation. Journal of Hazardous Materials, 387: 121701

Zhao S, Chen C, Ding J, Yang S, Zang Y, Ren N (2022). One-pot hydrothermal fabrication of $BiVO_4$/Fe_3O_4/rGO composite photocatalyst for the simulated solar light-driven degradation of Rhodamine B. Frontiers of Environmental Science & Engineering, 16(3): 36

Zheng K, Sun Y, Gong S, Jiang G, Zheng X, Yu Z (2019). Degradation of sulfamethoxazole in aqueous solution by dielectric barrier discharge plasma combined with Bi_2WO_6-rMoS_2 nanocomposite: mechanism and degradation pathway. Chemosphere, 222: 872–883

Zhou Y, Zhou L, Zhou Y, Xing M, Zhang J (2020). Z-scheme photo-Fenton system for efficiency synchronous oxidation of organic contaminants and reduction of metal ions. Applied Catalysis B: Environmental, 279: 119365

Zhu J, Wang J, Shan C, Zhang J, Lv L, Pan B (2019a). Durable activation of peroxymonosulfate mediated by Co-doped mesoporous $FePO_4$ via charge redistribution for atrazine degradation. Chemical Engineering Journal, 375: 122009

Zhu M, Yang J E, Delai Sun D, Yuan B, Fu M (2022). Deciphering the simultaneous removal of carbamazepine and metronidazole by monolithic Co_2AlO_4@Al_2O_3 activated peroxymonosulfate. Chemical Engineering Journal, 436: 135201

Zhu S, Li X, Kang J, Duan X, Wang S (2019b). Persulfate activation on crystallographic manganese oxides: mechanism of singlet oxygen evolution for nonradical selective degradation of aqueous contaminants. Environmental Science & Technology, 53(1): 307–315